World Scientific Research Journal Volume 12 Issue 4, 2026
ISSN: 2472-3703 DOI: 10.6911/WSRJ.202604_12(4).0001

Meteorological Drought Prediction in the Loess Plateau Based on Three Machine Learning Models

Yingqiang Li, Yongfan Guo, Qingchi Yi, Yanli Pei, Qunqun Li, Wei Wei*

College of Geography and Environmental Science, Northwest Normal University, Lanzhou 730070, China

* Corresponding: weiwei@nwnu.edu.cn (W.Wei)

Abstract

Drought, a severe natural hazard, exerts profound impacts on both ecological systems and agricultural productivity. Consequently, advancing drought prediction methodologies is paramount for optimizing regional water resource management and mitigating associated risks. This research centers on the Loess Plateau, leveraging monthly precipitation (P) and potential evapotranspiration (PET) datasets spanning 1960 to 2022 to compute the Standardized Precipitation Index (SPI) and Standardized Precipitation Evapotranspiration Index (SPEI) at temporal resolutions of 1-, 3-, 6-, and 12-months. The predictive efficacy of three computational models—Convolutional Long Short-Term Memory (CNN-LSTM), Random Forest (RF), and Support Vector Machine (SVM)—was systematically evaluated across semi-humid, semi-arid, and arid climatic zones. Empirical results elucidate three key findings: (1) CNN-LSTM outperformed its counterparts across all regions and time scales; RF demonstrated superior accuracy relative to SVM at 3- and 6-month lags, whereas SVM yielded stronger predictive power at the 12-month scale. Overall, the performance hierarchy prioritizes CNN-LSTM > RF > SVM for short-to-medium term forecasts, while CNN-LSTM > SVM > RF holds for long-term projections. (2) Model predictive accuracy achieved higher magnitudes when employing SPEI as the predictor compared to SPI within semi-arid and semi-humid domains. Conversely, in arid regions at extended time scales, SPI-12 outperformed SPEI-12, indicating that precipitation-dominated trends exhibit greater relevance for long-term drought forecasting in water-scarce areas. (3) Incorporating SPEI into the predictive framework conferred significantly enhanced performance in semi-arid and arid zones relative to semi-humid regions, further underscoring SPEI's utility in water-limited landscapes. Collectively, this study elucidates the interrelationships among model architectures, drought indices, and regional climatic characteristics, thereby establishing a scientific basis for developing regional drought early-warning systems and decision-support tools. These outcomes carry practical implications for optimizing agricultural management strategies and regulating water resources.

Keywords

Loess Plateau; drought prediction; SVM; RF; CNN-LSTM; SPI; SPEI.

1. INTRODUCTION

Drought represents a quintessential extreme climatic phenomenon, driven by the persistent imbalance between regional water availability and demand (Jiao et al., 2021). Against the backdrop of ongoing global climate change, both the frequency and severity of extreme climate events—most notably drought—have exhibited a pronounced upward trajectory in recent decades (Chiang et al., 2021). As documented by the Food and Agriculture Organization of the

ISSN: 2472-3703 DOI: 10.6911/WSRJ.202604_12(4).0001

United Nations (FAO), drought-induced economic losses globally reach approximately 250–300 billion USD annually, with projections indicating this burden will continue to escalate in the coming years (Xu et al., 2021a).

At the continental scale, sea surface temperature (SST) anomalies in tropical and subtropical ocean basins—particularly the interannual climate oscillations in the Pacific and Indian Oceans, namely El Niño and La Niña—exert profound regulatory effects on China's climate system. El Niño events are typically associated with significant precipitation deficits across northern and northwestern China, while La Niña conditions often exacerbate drought intensity in the northwestern region. Furthermore, large-scale atmospheric circulation anomalies, such as the South Asian High and Arctic Oscillation, can reshape regional water balance patterns across diverse temporal scales, thereby modifying the occurrence frequency and severity of drought events (Dixit & Jayakumar, 2021). These processes, which are jointly driven by global climate anomalies and regional atmospheric circulation dynamics, interact with local hydrological regimes and underlying surface properties, rendering the mechanisms governing drought onset and evolution increasingly complex. This complexity poses substantial challenges to accurate drought monitoring, early warning systems, and the development of effective disaster prevention and mitigation strategies (Buttafuoco et al., 2015).

Drought is conventionally classified into four primary categories: meteorological drought, hydrological drought, agricultural drought, and socio-economic drought (Mishra & Singh, 2010). The progression of drought constitutes a complex process driven by sustained precipitation deficits, where meteorological drought originates from anomalous climatic conditions characterized by insufficient rainfall and elevated evaporative demand. This initial deficit triggers soil moisture depletion, which may ultimately escalate into agricultural and hydrological drought events (Xu et al., 2021b). As a multifaceted natural phenomenon, the onset and evolution of meteorological drought are increasingly modulated by ongoing climate change (Manzano et al., 2019; Zhang et al., 2022), presenting formidable challenges to global water resource governance and disaster risk reduction. Imbalances within the hydrological cycle frequently give rise to diverse manifestations of meteorological drought, such as pronounced precipitation reductions or intensified evapotranspiration (Acharki et al., 2023; Alsubih et al., 2021). In contrast to abrupt natural disasters, meteorological drought develops and propagates gradually across extensive spatial and temporal domains, exhibiting highly nonlinear behavioral characteristics (Mishra & Singh, 2010; Wu et al., 2022). Its occurrence and severity are not only shaped by fluctuations in meteorological variables including precipitation and temperature but also jointly constrained by geographical and environmental factors, such as topographic heterogeneity, land use configurations, and soil properties. Consequently, in regions characterized by highly complex climate and environmental systems, the accurate modeling and prediction of the spatiotemporal evolution of meteorological drought remains a substantial scientific challenge (Li et al., 2021). For this reason, the present study centers on the prediction of meteorological drought, a task of critical significance for emergency management, drought risk mitigation, and the reduction of economic losses.

Drought severity is routinely evaluated through a suite of specialized drought indices (Mishra & Singh, 2010). Among these metrics, the Standardized Precipitation Index (SPI; McKee et al., 1993) and the Standardized Precipitation Evapotranspiration Index (SPEI; Vicente-Serrano et al., 2010) stand as the most extensively utilized indicators for meteorological drought monitoring. In contrast to SPI, SPEI integrates the influence of potential evapotranspiration, enabling it to capture the multifaceted characteristics of meteorological drought across a spectrum of temporal scales. For example, the 12-month SPEI is commonly employed to characterize interannual drought variability (Schreiner-McGraw & Ajami, 2021), the 6-month SPEI is well-suited for reflecting drought conditions throughout the crop growing season (April to September) (Potop et al., 2014), and the 3-month SPEI is primarily applied to delineate

ISSN: 2472-3703 DOI: 10.6911/WSRJ.202604_12(4).0001

seasonal drought patterns (Xu et al., 2021c). Given that meteorological drought typically precedes the onset of agricultural and hydrological drought, its quantitative prediction not only streamlines the early detection of drought risk but also contributes to mitigating economic losses in agricultural production and water resource management.

Drought forecasting serves as a cornerstone of drought risk governance, with its core objective being to deliver scientific underpinnings for early warning systems, thereby mitigating potential adverse impacts on agricultural production and ecological systems (Yuan et al., 2017). Prevalent methodologies for drought prediction encompass data-driven models (Xu et al., 2020), regression frameworks (Sun et al., 2012), conditional probability approaches (Hao et al., 2016), and machine learning algorithms (Xu et al., 2022), each characterized by distinct advantages and limitations. In recent years, driven by the rapid advancement of machine learning technologies, hybrid data-driven models that integrate machine learning and deep learning have emerged as promising analytical tools, owing to their relative ease of development and reduced input variable requirements (Almikaeel et al., 2022). In comparison to conventional machine learning techniques, deep learning models have demonstrated superior efficacy and have been extensively deployed in climate change analysis, land-use and land-cover change detection, and drought monitoring. The most widely adopted deep learning architectures include Convolutional Neural Networks (CNNs) and Recurrent Neural Networks (RNNs). Hybrid deep learning models, which fuse CNNs with Long Short-Term Memory (LSTM) networks, have been developed to enhance the consistency of drought monitoring and prediction (Le Cun et al., 2015).

Recent research underscores the expanding diversity of model applications. Shahnazi et al. (2025) advanced groundwater drought forecasting by developing an advanced integrated GWO-SVM model, utilizing the Standardized Groundwater Level Index (SGI) to monitor drought conditions in a critical aquifer in Iran and predict drought across multiple temporal horizons. Xu et al. (2025) achieved accurate sea ice drift prediction using a Self-Attention Convolutional LSTM Network (SaCLN). Zhang et al. (2024) employed ConvLSTM to forecast short-term meteorological drought in China, attaining an R^2 of 0.8 and generating valuable insights for short-term drought prediction. Hou et al. (2024) integrated the ARIMA model with BiLSTM to construct an ARIMA-BiLSTM hybrid model for drought prediction in Jilin Province, demonstrating that the combined model significantly outperformed individual models in terms of prediction accuracy. Belayneh et al. (2014) compared traditional stochastic models (ARIMA), Artificial Neural Networks (ANNs), and Support Vector Regression (SVR), revealing that ANNs exhibited superior performance relative to the other two methods. Şener and Tuğal (2025) successfully predicted solar radiation using the RF model. More recently, Zhang et al. (2025) proposed a novel CNN-BiLSTM-Attention hybrid model that captures both short-term fluctuations and long-term trends under complex marine conditions—including wind variability, temperature gradients, and atmospheric pressure changes—thereby enhancing forecasting adaptability across multiple temporal scales and improving the accuracy of offshore wind power prediction.

The Loess Plateau is distinguished by intricate climatic conditions, heterogeneous spatiotemporal patterns of precipitation, fragile ecological systems, and heightened sensitivity to climate change (Zhang et al., 2012). Variations in temperature and precipitation exert significant asymmetric impacts on vegetation growth and drought dynamics, with these effects exhibiting distinct manifestations across diverse climatic zones and ecosystems—offering novel perspectives for meteorological drought prediction and ecological management (He et al., 2023; He et al., 2024; He et al., 2025). Under the context of global warming, the region is confronted with intensifying drought and the consequent ecological and agricultural challenges, rendering accurate meteorological drought forecasting particularly imperative. Given its extensive

ISSN: 2472-3703 DOI: 10.6911/WSRJ.202604_12(4).0001

geographic scope, the present study partitions the Loess Plateau into semi-arid, arid, and semi-humid sub-regions to enable region-specific drought prediction.

However, a majority of existing domestic and international studies have predominantly centered on single-algorithm models and frequently rely on drought indices at a single temporal scale. Such methodologies lack comprehensive comparative evaluations across multiple models and time scales, and fail to capture the disparities in model performance under varying indices, temporal horizons, and climatic zones. To address these research gaps, this study utilizes the SPI and SPEI indices at 1-, 3-, 6-, and 12-month temporal scales, in conjunction with two conventional machine learning models (SVM and RF) and a hybrid deep learning model (CNN-LSTM), to forecast meteorological drought across the Loess Plateau. This research aims to identify (1) the optimal prediction model for each sub-region of the Loess Plateau, and (2) the most suitable drought index and temporal scale for each sub-region.

2. STUDY REGION AND DATA SOURCES

2.1. Introduction to the Study Area

Situated in north-central China (100°54′E–114°33′E, 33°43′N–41°16′N), the Loess Plateau constitutes one of the country's four major plateau landforms. Its spatial extent stretches westward to the Riyue Mountains in Qinghai, eastward to the Taihang Mountains, northward to the Great Wall in southern Inner Mongolia, and southward to the Qinling Mountains, encompassing parts of Shanxi, Shaanxi, Qinghai, Ningxia, Inner Mongolia, and Henan, with a total area of approximately 62.4×10^4 km^2. As a key component of China's second topographic step, the region exhibits a general topographic gradient of higher elevation in the northwest and lower elevation in the southeast, with the upper reaches of the Yellow River traversing its central and eastern portions (Fig. 1a) (Liu et al., 2016).

The Loess Plateau is dominated by a warm temperate continental monsoon climate, shaped by broad-scale monsoonal influences. Mean annual temperatures exhibit a distinct spatial gradient, ranging from 3.6 °C in the northwestern sector to 14.3 °C in the southeastern sector. The climate is characterized by pronounced diurnal temperature fluctuations, cold and arid winters, hot and humid summers, rapid cooling in autumn, and swift warming in spring. Mean annual potential evapotranspiration (865–1274 mm) consistently exceeds annual precipitation across the region (Li et al., 2012). Encompassing arid, semi-arid, and semi-humid climatic zones (Fig. 1b and Fig. 1c), the Loess Plateau is widely recognized as a climatically sensitive transitional zone between semi-arid and semi-humid environmental regimes (Liu & Sang, 2013).

2.2. Data Sources

The study area covers the entire Loess Plateau, with the study period spanning 1960–2022. The temporal resolution of the data was unified to one month, and the spatial resolution was set to 1 km. All raster data were clipped to the extent of the Loess Plateau using ArcMap 10.8 and projected to WGS_1984_UTM_Zone_49N. Based on this, monthly precipitation (PRE) and potential evapotranspiration (PET) data from 1960 to 2022 were used to calculate SPI and SPEI. A total of 756 raster images were generated at the 1-month scale, 754 at the 3-month scale, 751 at the 6-month scale, and 745 at the 12-month scale. Given the large data volume, which made direct computation infeasible, a 10 × 10 fishnet grid was constructed (Fig. 2), and raster images were converted into point data for processing. Ultimately, 3,642 data points were obtained for the semi-humid region, 743 for the semi-arid region, and 2,074 for the arid region.

In the calculation of SPI and SPEI, although traditional methods often require goodness-of-fit testing between the selected distribution (e.g., Gamma or log-logistic) and the observed data, the precipitation (PRE) and potential evapotranspiration (PET) datasets used in this study are

ISSN: 2472-3703 DOI: 10.6911/WSRJ.202604_12(4).0001

standardized products that have undergone strict quality control and validation. Therefore, SPI and SPEI were directly computed for the long-term series (1960–2022) using the Python-gma library, which incorporates built-in distribution fitting and standardization processes, ensuring theoretical consistency and producing results aligned with the standard definitions of drought indices. Consequently, no additional goodness-of-fit tests were performed, as the use of validated data products and a mature computational tool guarantees the reliability and comparability of the results.

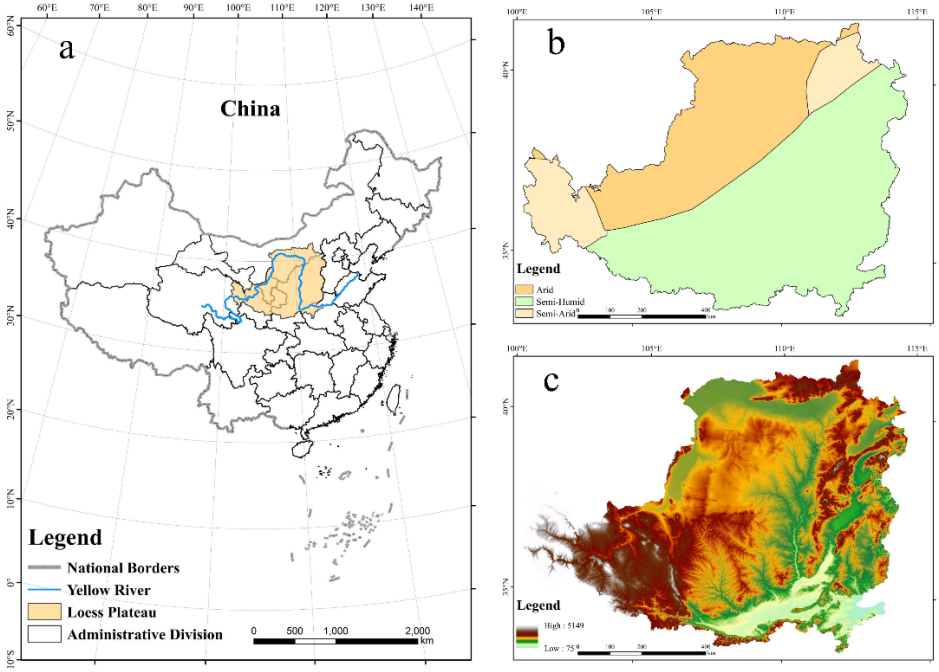

Figure 1. Location of the Study Area;(a) Geographical location of the Loess Plateau in China. (b) Aridity and humidity region of the Loess Plateau.(c) Digital Elevation Model of the Loess Plateau.

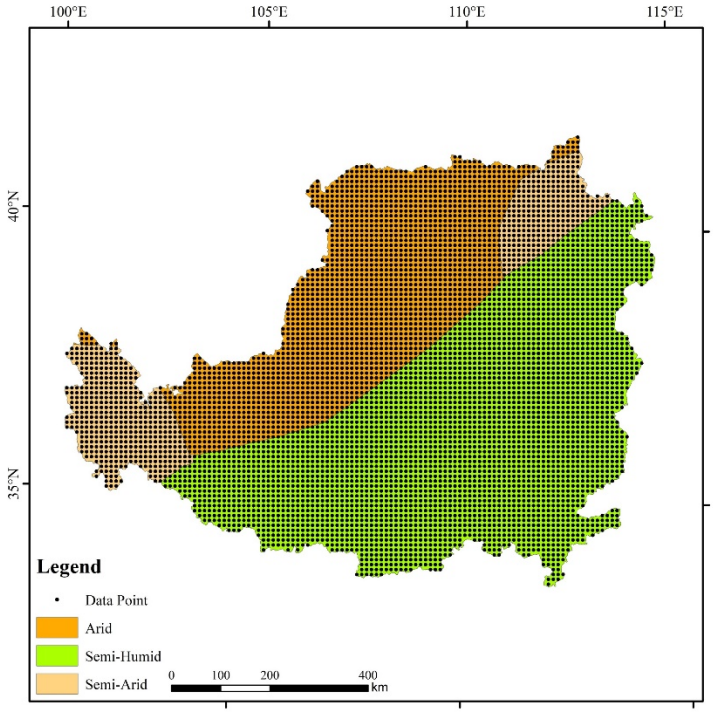

Figure 2. 10 km × 10 km fishnet grid division of the Loess Plateau study area.

ISSN: 2472-3703 DOI: 10.6911/WSRJ.202604_12(4).0001

2.2.1 Precipitation data

The precipitation (PRE) data were obtained from the National Tibetan Plateau Data Center (https://data.tpdc.ac.cn/). The dataset has a spatial resolution of 0.0083333° (approximately 1 km), a monthly temporal resolution, and is provided in raster format with units of millimeters. The temporal coverage spans 1960–2022, comprising a total of 756 raster images.

2.2.2 Potential evapotranspiration data

The potential evapotranspiration (PET) data were also obtained from the National Tibetan Plateau Data Center (https://data.tpdc.ac.cn/). The dataset has the same spatial resolution of 0.0083333° (approximately 1 km) and a monthly temporal resolution, provided in raster format with units of 0.1 mm. Its temporal coverage is 1960–2022, consisting of 756 raster images in total.

2.2.3 Climatic Zoning Data

The climatic zoning data were obtained from the Data Center for Resources and Environmental Sciences, Chinese Academy of Sciences (https://www.resdc.cn/). In this study, the Loess Plateau was divided into three sub-regions: semi-humid, semi-arid, and arid.

3. METHODOLOGY

3.1. Meteorological Drought Index

3.1.1 SPI

This study employs the probability density function of the Gamma distribution to fit precipitation data, obtaining the probability distribution of precipitation. The cumulative distribution function is then calculated based on the probability distribution and transformed into standardized normal distribution values, resulting in the corresponding SPI values. Mckee *et al*. (1993) used the Gamma distribution to describe the variability of precipitation distribution. Assuming the precipitation amount during a certain time period is x , its probability density function follows a Gamma distribution, the calculation formula is shown in equation (1):

$$f(x)=\frac{1}{\beta^{\alpha}\Gamma(\alpha)}x^{\alpha-1}e^{-x/\beta},x>0 \tag{1}$$

where $\alpha>0$ is the shape parameter, $\beta>0$ is the scale parameter, and $x>0$ represents the precipitation amount. $\Gamma(\alpha)$ is the Gamma function, and its probability density function is given by (2):

$$\Gamma(\alpha)=\int_0^{\infty}y^{\alpha-1}e^{-y}\,dy \tag{2}$$

In the equation, the estimated values of α、β are obtained using the Maximum Likelihood Estimation (MLE) method, calculated as (3):

ISSN: 2472-3703 DOI: 10.6911/WSRJ.202604_12(4).0001

$$\hat{\alpha} = \frac{1}{4A}\left(1+\sqrt{1+\frac{4A}{3}}\right)$$
$$\hat{\beta} = \frac{\overline{x}}{\hat{\alpha}} \tag{3}$$
$$A = \ln\left(\overline{x}\right) - \frac{\sum \ln\left(x_i\right)}{n}$$

where x_i represents the sample of the precipitation series, $\overline{x}$ is the mean of the precipitation series, and n is the length of the precipitation time series. Therefore, the cumulative probability for a given time period can be calculated using the following formula (4):

$$F\left(x\right) = \int_0^x f\left(x\right)dx = \frac{1}{\hat{\beta}^{\hat{\alpha}}\Gamma\left(\hat{\alpha}\right)}\int_0^x x^{\alpha-1}e^{-x/\hat{\beta}}dx \tag{4}$$

In the equation, the cumulative distribution function $F\left(x\right)$ is defined as the integral of the probability density function $f\left(x\right)$ from 0 to x, Substituting into formula (1) gives the above expression.

When the precipitation amount is $x = 0$, the probability density function of the Gamma distribution is not defined at $x = 0$ (since the domain of the Gamma distribution is $x > 0$). To address the case where the actual precipitation amount is zero, a correction method needs to be introduced (Husak *et al*., 2007). This is typically done by considering the probability of zero precipitation and incorporating it into the cumulative distribution function. Therefore, the corrected cumulative probability expression can be adjusted to the following form of equation (5):

$$H\left(x\right) = \begin{cases} q, & x = 0 \\ q + (1-q).F\left(x\right) & x > 0 \end{cases} \tag{5}$$

where q represents the probability of rainfall. Let m be the number of samples in the precipitation series where the value is 0, and n be the total number of samples. Then, we have $q = m/n$.

The probability density function of the standard normal distribution is given by (6):

$$\phi\left(x\right) = \frac{1}{\sqrt{2\pi}}e^{-z^2/2} \tag{6}$$

The cumulative distribution function $H\left(x\right)$ is the accumulated probability from $-\infty$ to x. The formula is shown in equation (7):

$$H\left(x\right) = \frac{1}{\sqrt{2\pi}}\int_{-\infty}^{x} e^{-t^2/2}\,dt \tag{7}$$

The approximation is obtained as follows:

ISSN: 2472-3703 DOI: 10.6911/WSRJ.202604_12(4).0001

When $0 < H(x) \le 0.5$ is negative, the SPI value indicates drought. The formula is shown in equation (8).

$$SPI = -\left(t - \frac{c_0 + c_1 t + c_2 t^2}{1 + d_1 t + d_2 t^2 + d_3 t^3} \right)$$
$$t = \sqrt{\ln\left(\frac{1}{(H(x))^2} \right)} \tag{8}$$

When $0.5 < H(x) < 1$ is greater than the median, the precipitation probability is higher, corresponding to wet conditions, and the SPI value is positive. The formula is shown in equation (9).

$$SPI = \left(t - \frac{c_0 + c_1 t + c_2 t^2}{1 + d_1 t + d_2 t^2 + d_3 t^3} \right)$$
$$t = \sqrt{\ln\left(\frac{1}{(1.0 - H(x))^2} \right)} \tag{9}$$

Where t is an intermediate variable used to calculate the SPI. $c_0, c_1, c_2, d_1, d_2, d_3$ represents the empirical parameters derived from the standard normal distribution. According to the literature, the standard values for these parameters are as follows (Mckee *et al.*,1993):
$c_0 = 2.515517, c_1 = 0.802853, c_2 = 0.010328, d_1 = 1.432788, d_2 = 0.189269, d_3 = 0.001308$

3.1.2 SPEI

The Standardized Precipitation Evapotranspiration Index (SPEI) depends on the variation in the difference between precipitation and potential evapotranspiration (PET). Common methods include the Penman-Monteith method, the Thornthwaite method, and the Hargreaves method. Among these, the Hargreaves method, based on the monthly average temperature, maximum temperature, and minimum temperature, is used to calculate the monthly PET (Hargreaves and Samani, 1982). In this study, Hargreaves and Samani (1985) developed the improved formula to enhance the accuracy of PET estimation, providing reliable data support for subsequent SPEI calculations. The formula is shown in equation (10):

$$PET = 0.0023 \times S_0 \times \left(T_{\max} - T_{\min} \right)^{0.5} \times \left(T_{mean} + 17.8 \right) \tag{10}$$

where $T_{\max}$ is the maximum air temperature of the month, $T_{\min}$ is the minimum air temperature of the month, T_{mean} is the average air temperature of the month, and S_0 is the extraterrestrial solar radiation at the top of the Earth's atmosphere on a horizontal surface (mm/month) (Allen et al., 1998). The specific calculation method for S_0 is described by Allen et al. (1998) and Zhao et al.(2004).

With the PET value, the difference between precipitation P and PET for the month i is given by (11):

$$D_i = P_i - PET_i \tag{11}$$

ISSN: 2472-3703 DOI: 10.6911/WSRJ.202604_12(4).0001

where D_i represents the base data for calculating the SPEI, indicating the moisture balance. When $D_i > 0$ indicates moisture surplus, $D_i < 0$ indicates moisture deficit. The summary of D_i values for different time scales is calculated, with the difference in $D_{i,j}^k$ values for the j-th month of year i depending on the selected time scale k. The calculation formula for $D_{i,j}^k$ is as follows (12):

$$\begin{aligned} D_{i,j}^k &= \sum_{m=13-k+j}^{12} D_{i-1,m} + \sum_{m=1}^{j} D_{i,m} \quad j < k \\ D_{i,j}^k &= \sum_{m=j-k+1}^{j} D_{i,m} \quad j \geq k \end{aligned} \tag{12}$$

where i represents the year, j represents the month, k is the accumulated time scale (such as 3 months, 6 months, 12 months, etc.), m is the cycle variable, indicating the month index. $\sum_{m=13-k+j}^{12} D_{i-1,m}$ represents the total moisture surplus or deficit from month $13-k+j$ to the end of December. $\sum_{m=1}^{i} D_{i,m}$ represents the total moisture surplus or deficit from January of the current year to month j.

After obtaining the D_i value, this study uses the log-logistic distribution to fit the logarithmic sequence D_i. The probability density function of the log-logistic distribution is calculated as (13):

$$f(x) = \frac{\beta}{\alpha}\left(\frac{x-\gamma}{\alpha}\right)^{\beta-1}\left[1+\left(\frac{x-\gamma}{\alpha}\right)^{\beta}\right]^{-2} \tag{13}$$

where α is the scale parameter, β is the shape parameter, and γ is the location parameter. The parameters of the log-logistic distribution can be calculated using different methods, among which the L-moment estimation is the most robust and simple. The formula is shown in equation (14):

$$\begin{aligned} \beta &= \frac{2w_1 - w_0}{6w_1 - w_0 - 6w_2} \\ \alpha &= \frac{(w_0 - 2w_1)\beta}{\Gamma(1+1/\beta)\Gamma(1-1/\beta)} \\ \gamma &= w_0 - \alpha\Gamma\left(1+\frac{1}{\beta}\right)\Gamma\left(1-\frac{1}{\beta}\right) \end{aligned} \tag{14}$$

where $\Gamma(\beta)$ is the Gamma distribution function of β. This results in the cumulative distribution function of D_i, the formula is shown in equation (15):

$$F(x) = \left[1+\left(\frac{\alpha}{x-\gamma}\right)^{\beta}\right]^{-1} \tag{15}$$

ISSN: 2472-3703 DOI: 10.6911/WSRJ.202604_12(4).0001

Then, the cumulative distribution function is standardized to a normal distribution, resulting in the time series of the SPEI, the formula is shown in equation (16):

$$SPEI = W - \frac{C_0 + C_1 W + C_2 W^2}{1 + d_1 W + d_2 W^2 + d_3 W^3}$$
$$W = \sqrt{-2\ln(P)} \quad for \quad P \le 0.5 \tag{16}$$

where P is the probability exceeding the D value, W is the probability-weighted distance, and $P = 1 - F(x)$. If $P > 0.5$, this P will be replaced by $1 - P$, and then the opposite value of the SPEI result will be taken, the formula is shown in equation (17):

$$SPEI = -\phi^{-1}(P) \tag{17}$$

Due to the presence of the negative sign, the result is the same as the original PP value. The values for P=0.2 and P = 0.8 are identical. The parameter values are as follows:

$$C_0 = 2.515517, C_1 = 0.802853, C_2 = 0.010328, d_1 = 1.432788,$$
$$d_2 = 0.189269, and\ d_3 = 0.001308$$

3.2. Drought Prediction Model

3.2.1 Random Forest

Random Forest (RF) is an ensemble learning method under the framework of supervised learning. Its basic idea is to improve prediction accuracy and stability by constructing and combining multiple decision trees (Feng et al., 2019). In implementation, RF mainly consists of two components: training sample subsets and base models. Using the bootstrap method, random samples with replacement are drawn from the original training set to generate multiple training subsets, and each subset is used to train one decision tree as a base learner. Based on M subsets, M independent decision trees can be generated, each providing a prediction result. The final output of the forest is then obtained by aggregating all decision tree results (Fig. 3). RF can be applied to both classification and regression tasks: in classification, the final class of a test sample is determined by majority voting across all trees, while in regression, the final prediction is the arithmetic mean of the outputs from all trees. Since different tasks require varying tree structures, depths, and splitting strategies, selecting appropriate parameters is a key issue in RF applications.

In this study, the RF model was employed to predict drought indices. Supervised learning samples were constructed using a sliding-window approach (input window length k=15, prediction lag z=1). After removing missing values, the dataset was strictly divided into training and testing sets in chronological order with a ratio of 70% to 30%. To eliminate the influence of scale differences, both input features and target variables were normalized to the [0,1] range using min–max normalization, and inverse transformation was applied after prediction. The model was implemented with the TreeBagger regression forest, using 100 trees and a minimum leaf size of 5. Out-of-Bag (OOB) prediction was enabled to evaluate generalization error, and OOB permuted predictor importance was used to measure the contribution of each input feature. Model performance was assessed using R^2, RMSE, and MAE for both the training and testing sets, supplemented by OOB error curves and feature importance analysis for further validation.

ISSN: 2472-3703 DOI: 10.6911/WSRJ.202604_12(4).0001

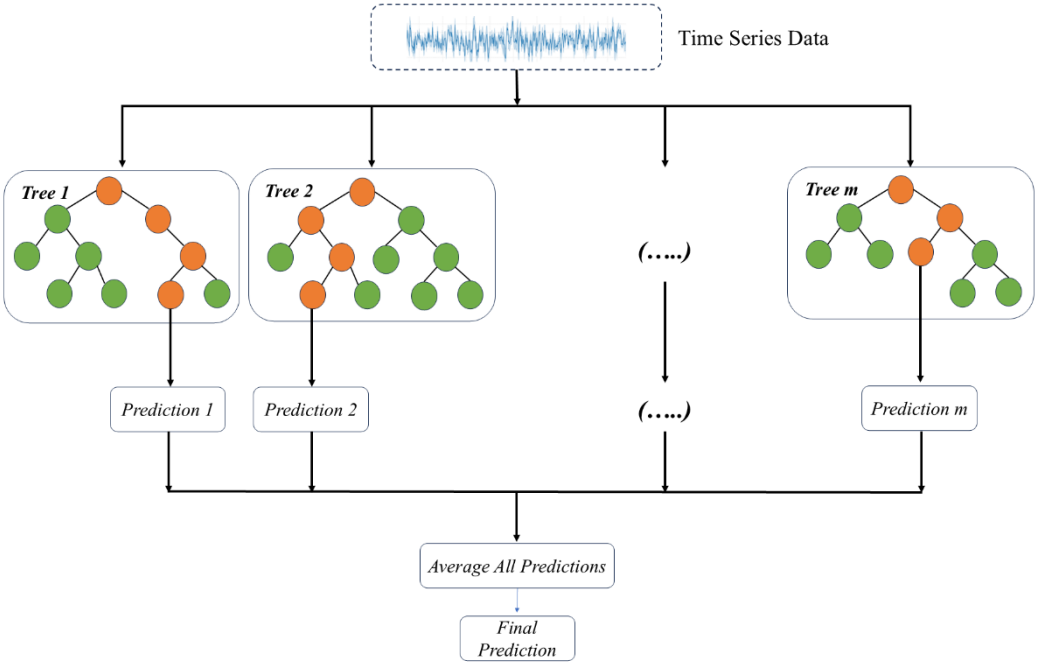

Figure 3. Random Forest regression.

3.2.2 Support Vector Machine

Support Vector Machine (SVM), proposed by Cortes et al. (1995), is a machine learning method that can be categorized into Support Vector Classification (SVC) for classification tasks and Support Vector Regression (SVR) for regression tasks. SVR aims to identify a function that deviates from the actual output by no more than a specified loss function (ε-insensitive zone), thereby reducing the risk of overfitting by balancing error tolerance and function flatness (Fig. 4).In this study, the SVR model was employed to predict drought indices, with the Radial Basis Function (RBF) selected as the kernel. Supervised learning samples were constructed using a sliding-window approach (input window length k=15, prediction lag z=1). After removing missing values, the dataset was split chronologically into training and testing sets with a ratio of 70% to 30%. Both input features and target variables were normalized to the [0,1] range using min–max scaling, and inverse transformation was applied after prediction. The SVM model was configured as ε-SVR, with penalty parameter C=4.0, kernel parameter γ=0.8，ε=0.01, which were empirically set and kept consistent across experiments.The basic principle of SVR can be described as follows: given a training dataset $D=\{(x_1,y_1),(x_2,y_2),\ldots,(x_l,y_l)\}\subset \aleph\times R,\aleph$, represents the input space, R represents the output space, and D denotes the training set, containing l samples. The objective of Support Vector Regression is to construct a function $f(x)$ such that, for each input sample x_i, the model's output $f(x_i)$ is as close as possible to the true target value y_i. SVR introduces a tolerance parameter ε, which allows errors within a certain range to remain unpenalized, thereby making the model more flexible. The model aims to minimize the loss function while keeping the complexity of the model as low as possible. In SVR, this is typically achieved by solving the following optimization problem to minimize the loss function, the formula is shown in equation (18):

$$\min_{\omega,b,\xi_i,\xi_i^*}\left(\frac{1}{2}\|\omega\|^2+C\sum_{i=1}^{l}\left(\xi_i+\xi_i^*\right)\right) \tag{18}$$

ISSN: 2472-3703 DOI: 10.6911/WSRJ.202604_12(4).0001

where ω is the weight vector of the regression model, which measures the importance of each feature in the prediction; b is the bias term of the model; ξ_i, ξ_i^* represents the slack variables, which indicate the errors; and C is the regularization parameter, used to control the balance between error and model complexity. Additionally, the following constraints apply, the formula is shown in equation (19):

$$\begin{aligned} & y_i - \left(\omega.\phi\left(x_i\right)+b\right) \le \varepsilon + \xi_i \\ & \left(\omega.\phi\left(x_i\right)+b\right) - y_i \le \varepsilon + \xi_i^* \\ & \xi_i, \xi_i^* \ge 0, \qquad i = 1,2,...,l \end{aligned} \tag{19}$$

Through the optimization problem mentioned above, SVR finds the optimal ω, b, thereby obtaining the regression model, the formula is shown in equation (20):

$$f\left(x\right) = \omega.\phi\left(x\right)+b \tag{20}$$

where $\phi\left(x\right)$ represents the mapping of the input vector x into a higher-dimensional space (achieved through the kernel function for nonlinear mapping), and $f\left(x\right)$ is the predicted value of the model for the input x. SVR constructs the regression model $f\left(x\right)$ by learning from the data in the training set, and fits the data by optimizing the objective function, ultimately predicting the output for unknown samples.

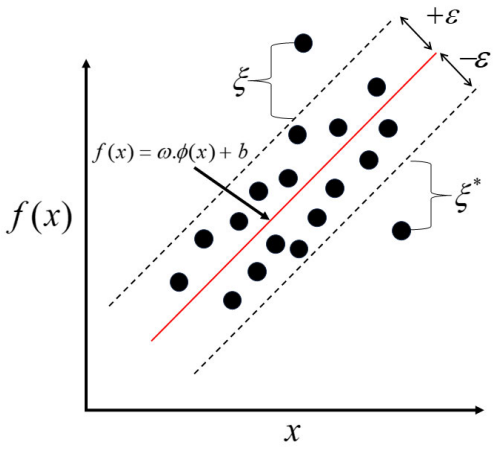

Figure 4. One-dimensional SVR.

3.2.3 CNN-LSTM

In this study, a deep learning prediction model combining Convolutional Neural Networks (CNN) and Long Short-Term Memory (LSTM) networks (CNN-LSTM) was employed, with the architecture shown in Fig. 5. The raw time series data were first processed by one-dimensional convolution operations to extract local temporal features, with the ReLU activation function enhancing nonlinear representation capability. MaxPooling was then applied for feature dimensionality reduction and redundancy compression, generating more representative high-level features. These features were subsequently fed into the LSTM module, where gated mechanisms—namely the input gate, forget gate, and output gate—dynamically regulated

ISSN: 2472-3703 DOI: 10.6911/WSRJ.202604_12(4).0001

information flow, effectively filtering irrelevant information while capturing long-range dependencies and dynamic evolution characteristics. After mapping through a fully connected layer, the model produced the prediction results (Zhang et al., 2023). This hybrid architecture leverages the strengths of both CNN and LSTM: CNN extracts discriminative patterns from local temporal domains, reducing noise and redundancy in the raw time series, while LSTM characterizes long-term dependencies and non-stationary dynamics. The combination ensures robust local pattern recognition and enhanced global dependency modeling, thereby improving the accuracy and stability of complex time series prediction.

In implementation, supervised learning samples were constructed using a sliding-window method, and the sequences were divided strictly in chronological order into training, validation, and testing sets (63%/7%/30%). Both features and targets were normalized using min–max scaling. The model architecture consisted of two layers of one-dimensional convolution with ReLU activation, an LSTM layer (64 units, output mode set to "last"), and a fully connected regression output. The optimizer was Adam with an initial learning rate of 1×10^{-3}, a batch size of 32, and the mean squared error (MSE) loss function. To mitigate overfitting, Dropout layers (rate = 0.2) were added after both the convolution and LSTM layers, combined with L2 weight regularization and gradient clipping. An early stopping strategy was applied (patience = 6, i.e., training was terminated if the validation loss did not improve for six consecutive evaluations), together with a step learning rate scheduler (halving the learning rate every 5 epochs) to enhance training stability and generalization performance. Hyperparameters were tuned within a reasonable range using random and Bayesian search, with the validation RMSE as the selection criterion. A fixed random seed was used to ensure reproducibility of results.

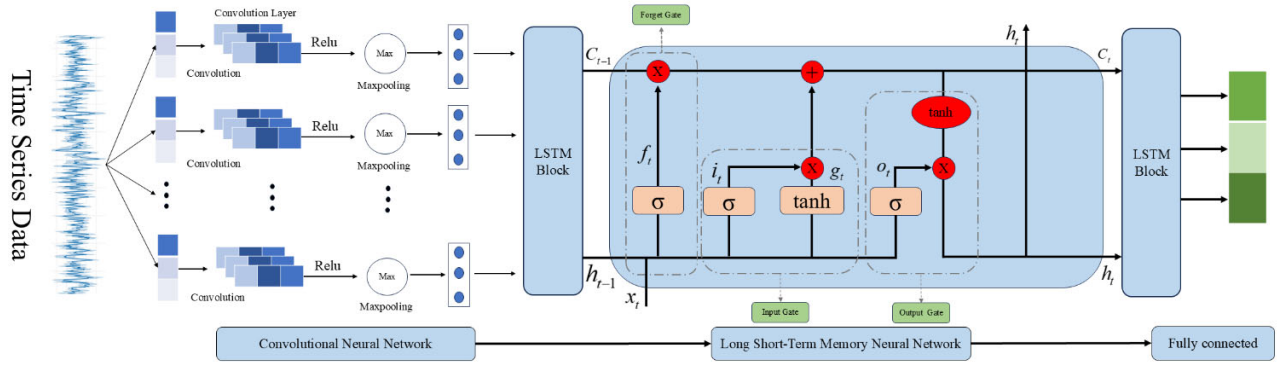

Figure 5. Architecture of the CNN-LSTM hybrid model

3.3. Model performance evaluation metrics

To evaluate the accuracy of the models on the testing set, three metrics were employed: the coefficient of determination R^2, the root mean square error $RMSE$, and the mean absolute error MAE. The value of R^2 ranges from –1 to 1, with values closer to 1 indicating better model fit, while smaller $RMSE$ and MAE values indicate better prediction performance (Zhao et al., 2021). The calculation formulas for the three metrics are as follows (21-23).

$$R^2 = 1 - \frac{\sum_{i=1}^{n}(y_i - \hat{y}_i)^2}{\sum_{i=1}^{n}(y_i - \bar{y})^2} \tag{21}$$

ISSN: 2472-3703 DOI: 10.6911/WSRJ.202604_12(4).0001

$$RMSE = \sqrt{\frac{1}{n}\sum_{i=1}^{n}(y_i - \hat{y}_i)^2} \tag{22}$$

$$MAE = \frac{1}{n}\sum_{i=1}^{n}|y_i - \hat{y}_i| \tag{23}$$

where n represents the number of samples, $y_i, \hat{y}_i, \overline{y}$ correspond to the actual values, predicted values, and the mean of the actual values, respectively.

4. RESULT

This study employed three widely used machine learning methods for drought prediction: Support Vector Machine (SVM), Random Forest (RF), and Convolutional Neural Network–Long Short-Term Memory (CNN-LSTM). SVM is capable of constructing optimal decision boundaries in high-dimensional spaces, effectively handling nonlinear relationships, and demonstrating strong robustness in drought prediction. RF, as an ensemble learning method, integrates multiple decision trees to achieve high-accuracy predictions of complex data, particularly suitable for high-dimensional datasets. The CNN-LSTM model combines the spatial feature extraction capability of CNN with the temporal modeling strength of LSTM, enabling a more comprehensive characterization of the spatiotemporal dynamics of drought evolution. The results indicate that the prediction accuracy of all three models improves as the time scale of SPI and SPEI increases. When comparing predictive performance across different climatic regions (arid, semi-arid, and semi-humid), the CNN-LSTM model consistently achieves the best results across all regions and time scales. It should be noted, however, that at the 1-month scale, both SPI and SPEI exhibit large fluctuations, leading to generally poor predictive performance for all models; therefore, detailed discussion of results at this scale is omitted in this paper.

4.1. Prediction results based on RF model

Fig. 6 presents the predictive performance of the Random Forest (RF) model for SPI and SPEI across different climatic regions and time scales. The results reveal pronounced temporal-scale dependence and regional heterogeneity in drought prediction over the Loess Plateau. At the 1-month scale, predictive performance was generally poor, with most R^2 values close to zero or even negative, indicating limited capacity to capture short-term climate variability; hence, results at this scale are not discussed in detail. Starting from the 3-month scale, model performance improved gradually. For example, in the arid region, the R^2 values of SPI-3 and SPEI-3 increased to 0.31 and 0.33, respectively; however, the errors remained relatively high, with MAE ranging from 0.59 to 0.63 and RMSE between 0.74 and 0.78, reflecting limited capability in modeling short-term fluctuations.

As the time scale extended to 6 and 12 months, predictive accuracy improved markedly. At the 12-month scale, the R^2 values of SPI in the semi-arid, arid, and semi-humid regions reached 0.71, 0.79, and 0.72, respectively, while those of SPEI were 0.80, 0.76, and 0.72. Corresponding MAE values decreased to 0.26–0.30, with RMSE controlled within 0.37–0.42, indicating high reliability of the model for medium- and long-term predictions. Furthermore, in semi-arid and arid regions, the R^2 of SPEI at the 3-, 6-, and 12-month scales was consistently higher than that in the semi-humid region, whereas SPI did not exhibit such a pattern. This suggests that evapotranspiration plays a more critical role in climate prediction in water-limited regions, thereby highlighting the advantages of SPEI in arid and semi-arid environments. Overall, while the RF model shows limited effectiveness for short-term prediction, it achieves significantly

ISSN: 2472-3703 DOI: 10.6911/WSRJ.202604_12(4).0001

higher accuracy at medium- and long-term scales, particularly when combined with SPEI, thus providing more robust support for drought prediction in the Loess Plateau.

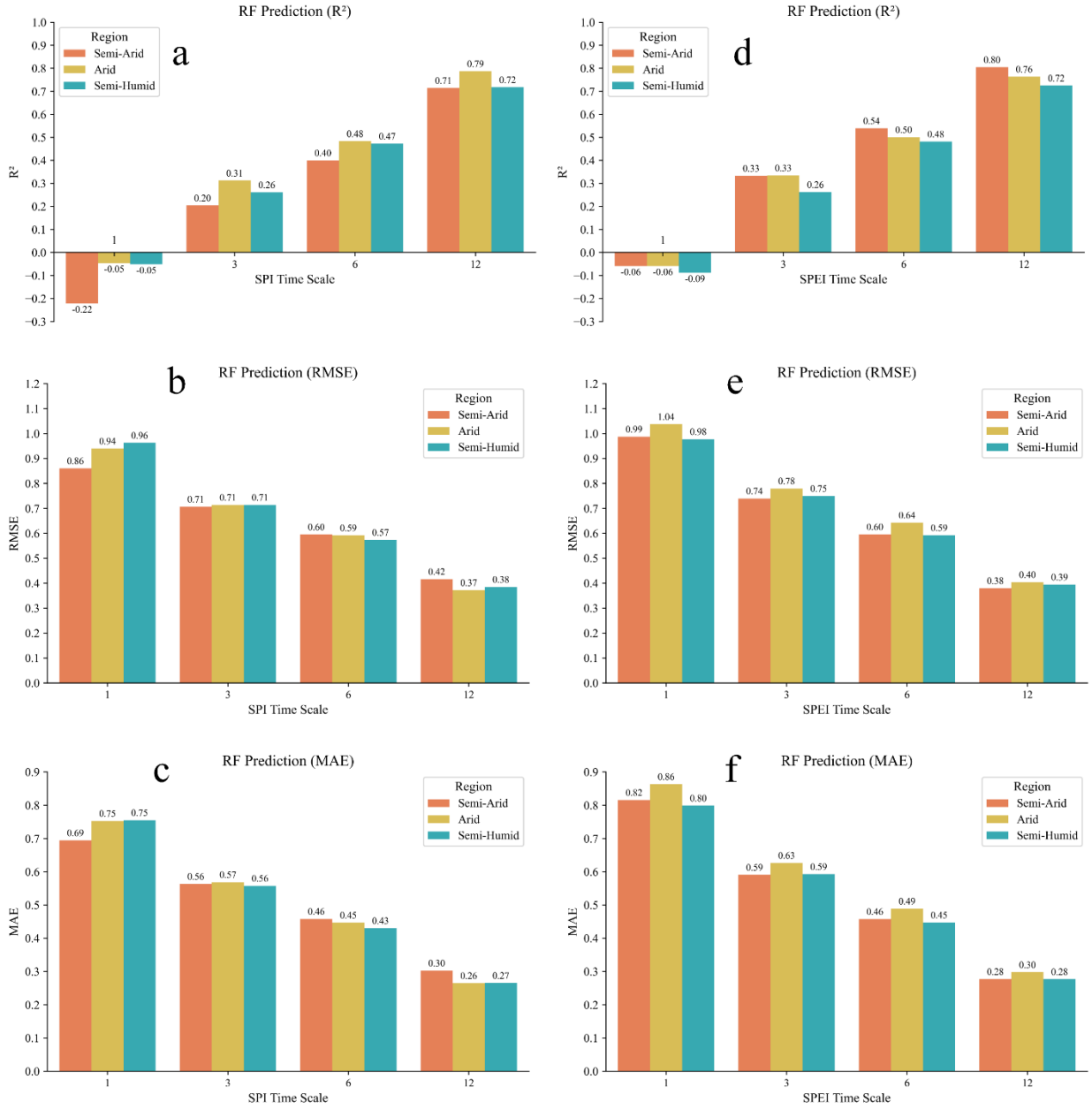

Figure 6. Predictive performance of the RF model: (a, d) coefficient of determination (R^2 ; (b, e) root mean square error (RMSE); (c, f) mean absolute error (MAE). The left column (a–c) shows results based on SPI, while the right column (d–f) shows results based on SPEI. The x-axis represents the time scales (1, 3, 6, and 12 months), and the y-axis represents the corresponding metric values.

4.2. Prediction results based on SVM model

The predictive performance of the Support Vector Machine (SVM) model for the Standardized Precipitation Index (SPI) and the Standardized Precipitation Evapotranspiration Index (SPEI) was evaluated across semi-humid, semi-arid, and arid regions of the Loess Plateau at different time scales (1, 3, 6, and 12 months). Fig. 7 illustrates the prediction performance of the SVM model in the semi-humid, semi-arid, and arid regions at these four time scales. The results show that the predictive capability of the SVM model was poor at the 1- and 3-month scales, with most R^2 values being negative or close to zero, indicating limited skill in forecasting short-term

ISSN: 2472-3703 DOI: 10.6911/WSRJ.202604_12(4).0001

meteorological drought. With increasing time scale, R^2 values improved while MAE and RMSE decreased significantly, reflecting a notable enhancement in predictive performance. In the semi-arid region, SPEI-12 and SPI-12 achieved R^2 values of 0.85 and 0.81, respectively, demonstrating the strongest performance.

The model also exhibited different predictive abilities across indices within the same region. In the arid region, SPI outperformed SPEI at medium- and long-term scales, while in the semi-arid region, SPEI was clearly superior to SPI (with SPEI-12 reaching an R^2 of 0.85 compared to 0.81 for SPI-12). In the semi-humid region, the performances of SPI and SPEI were similar. Notably, SPEI in the semi-arid and arid regions consistently outperformed that in the semi-humid region, whereas SPI did not display this pattern, further suggesting that evapotranspiration plays a crucial role in climate prediction in water-limited regions.

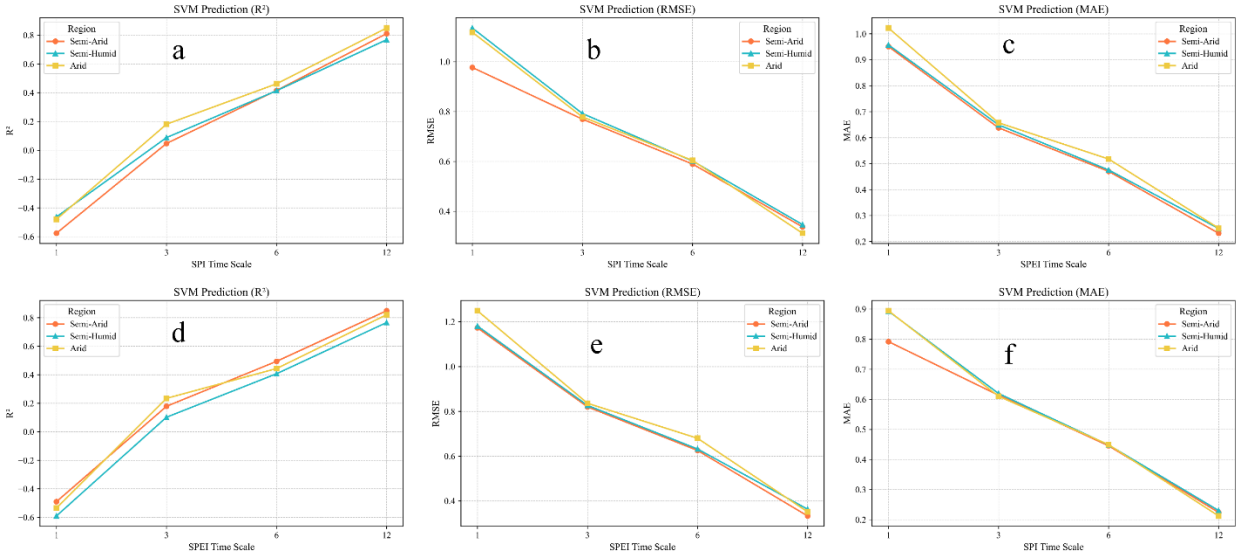

Figure 7. Predictive performance of the SVM model: top row (a–c) shows results based on SPI, including (a) coefficient of determination (R^2), (b) root mean square error (RMSE), and (c) mean absolute error (MAE); bottom row (d–f) shows results based on SPEI, including (d) R^2, (e) RMSE, and (f) MAE. The x-axis represents the time scales (1, 3, 6, and 12 months), and the y-axis represents the corresponding metric values.

4.3. Prediction results based on CNN-LSTM model

The CNN-LSTM model was employed to systematically evaluate the predictive performance of SPI and SPEI across semi-humid, semi-arid, and arid regions of the Loess Plateau at different time scales (1, 3, 6, and 12 months). Fig. 8 illustrates the model's prediction results across different regions and time scales. The results show that model performance improved substantially with increasing time scale, achieving the best accuracy at the 6- and 12-month scales. In particular, the R^2 values in the semi-arid and arid regions exceeded 0.80, while those in the semi-humid region reached 0.76–0.77. In contrast, prediction accuracy was relatively low at the 1- and 3-month scales, indicating that the CNN-LSTM model still has limitations in capturing short-term climate variability.

Moreover, compared with SPI-based predictions, the CNN-LSTM model exhibited consistently higher predictive accuracy when using SPEI across all three climatic regions. This finding highlights the value of incorporating evapotranspiration, which better characterizes regional water balance and thus enhances model applicability and predictive performance. Further comparison revealed that, when SPEI was used as the predictor, CNN-LSTM achieved higher

ISSN: 2472-3703 DOI: 10.6911/WSRJ.202604_12(4).0001

accuracy in semi-arid and arid regions than in the semi-humid region, underscoring the advantage of SPEI for meteorological drought prediction in water-limited environments.

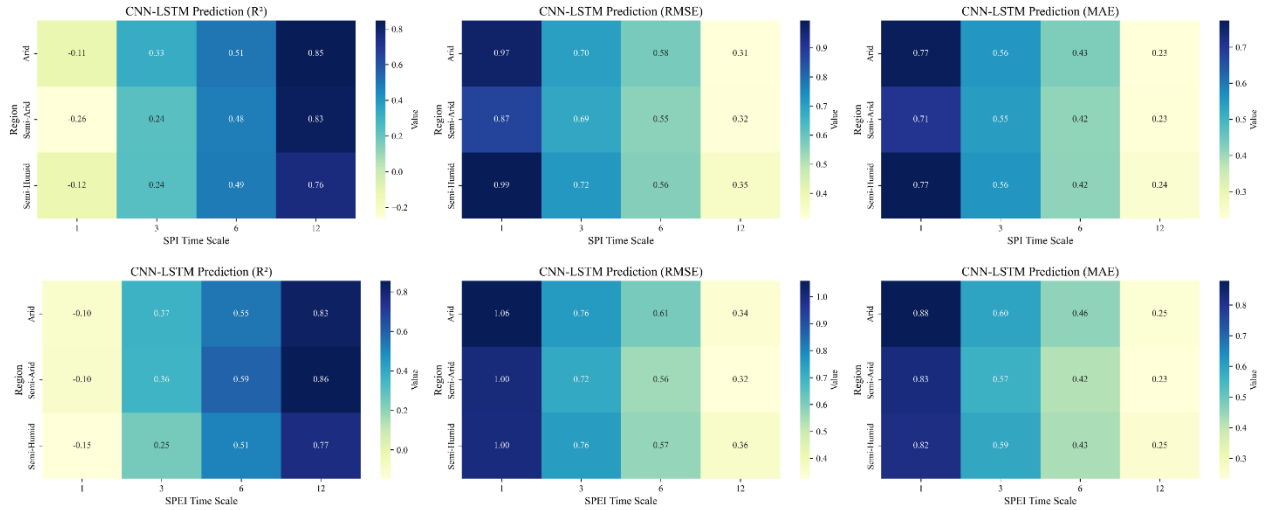

Figure 8. Heatmaps of CNN-LSTM model predictive performance: the top row shows results based on SPI, including coefficient of determination (R^2), root mean square error (RMSE), and mean absolute error (MAE); the bottom row shows results based on SPEI, including R^2 , RMSE, and MAE. The x-axis represents the time scales (1, 3, 6, and 12 months), the y-axis represents different regions, and the color shading indicates the magnitude of the metric values.

4.4. Comparison of Model Reliability

Across the three models, predictive performance was generally poor at short-term drought scales (1 and 3 months). This is primarily attributable to the high variability and complexity of short-term SPI and SPEI, as well as the non-stationary characteristics of the time series, which make it difficult for models to effectively capture underlying patterns. In particular, at the 1-month scale, the R^2 values of all three models were negative; therefore, this scale was excluded from subsequent performance comparisons. Fig. 9 and 10 present the predictive results of the three models for SPI and SPEI, respectively, across the arid, semi-arid, and semi-humid regions of the Loess Plateau.

The results show that the CNN-LSTM model consistently outperformed RF and SVM across all regions and time scales. At the 3- and 6-month short- to medium-term scales, the RF model generally performed better than SVM, whereas at the 12-month long-term scale, SVM significantly outperformed RF. Notably, the CNN-LSTM model maintained leading performance under all conditions. Its superiority stems from the complementary strengths of convolutional neural networks (CNNs), which effectively extract complex spatial features, and long short-term memory networks (LSTMs), which excel at capturing long-term dependencies in time series. As a result, CNN-LSTM demonstrates greater adaptability and robustness in drought prediction tasks characterized by strong spatiotemporal coupling, particularly achieving higher accuracy and stability in medium- to long-term forecasting. By contrast, SVM and RF show certain limitations in modeling long-term dependencies and dynamic changes in time series. Overall, the performance ranking was CNN-LSTM > RF > SVM at short- to medium-term scales (3 and 6 months), and CNN-LSTM > SVM > RF at the long-term scale (12 months).

ISSN: 2472-3703 DOI: 10.6911/WSRJ.202604_12(4).0001

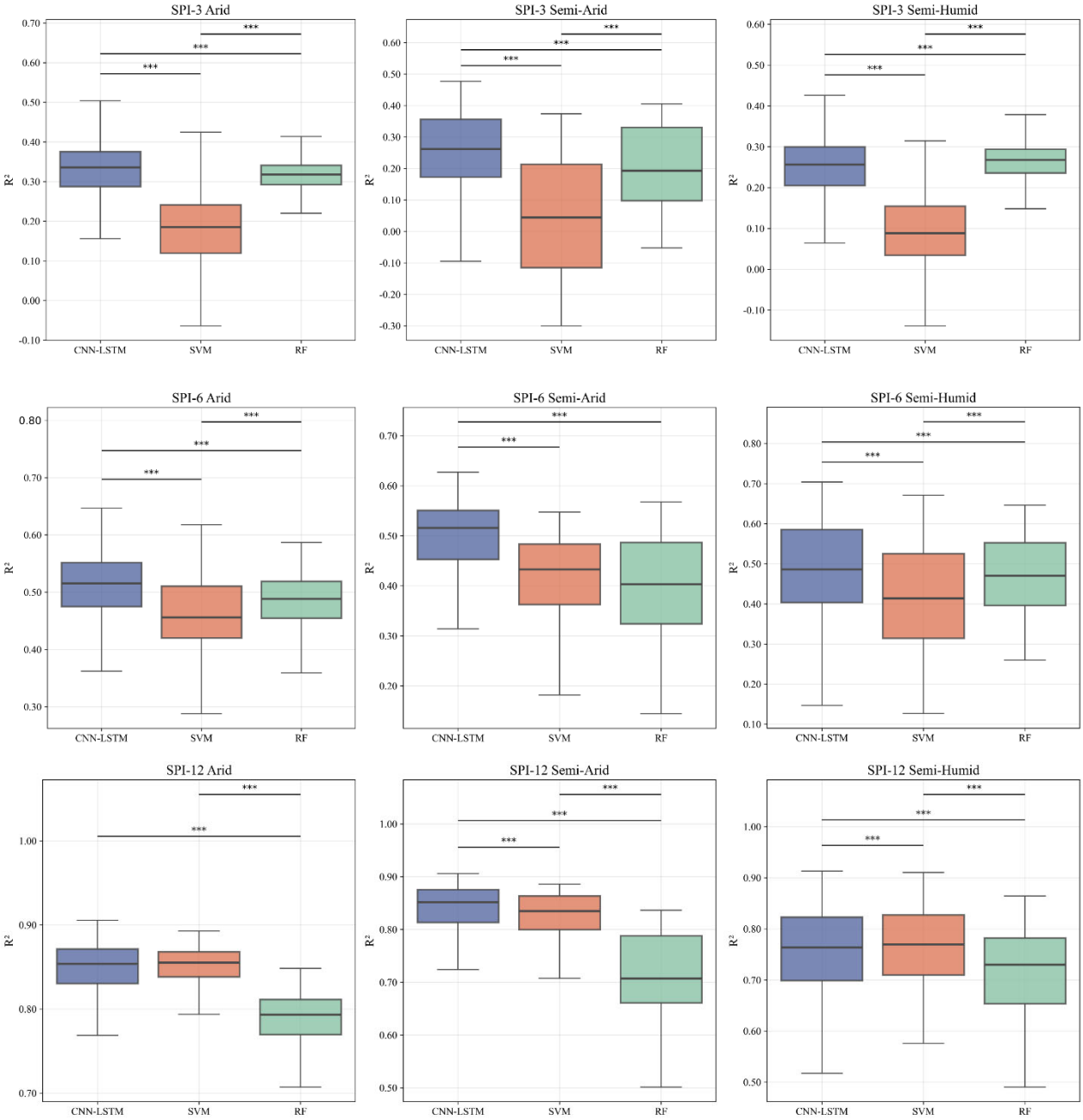

Figure 9. Comparison of predictive performance of the three models based on SPI at different time scales. From top to bottom: 3-month (SPI-3), 6-month (SPI-6), and 12-month (SPI-12) scales; from left to right: arid, semi-arid, and semi-humid regions. The boxplots show the distribution of R^2 values across models, including medians and variability ranges. Horizontal lines and asterisks (*, **, ***) indicate the significance levels of pairwise differences among models (*p<0.05, **p<0.01, ***p<0.001).

ISSN: 2472-3703 DOI: 10.6911/WSRJ.202604_12(4).0001

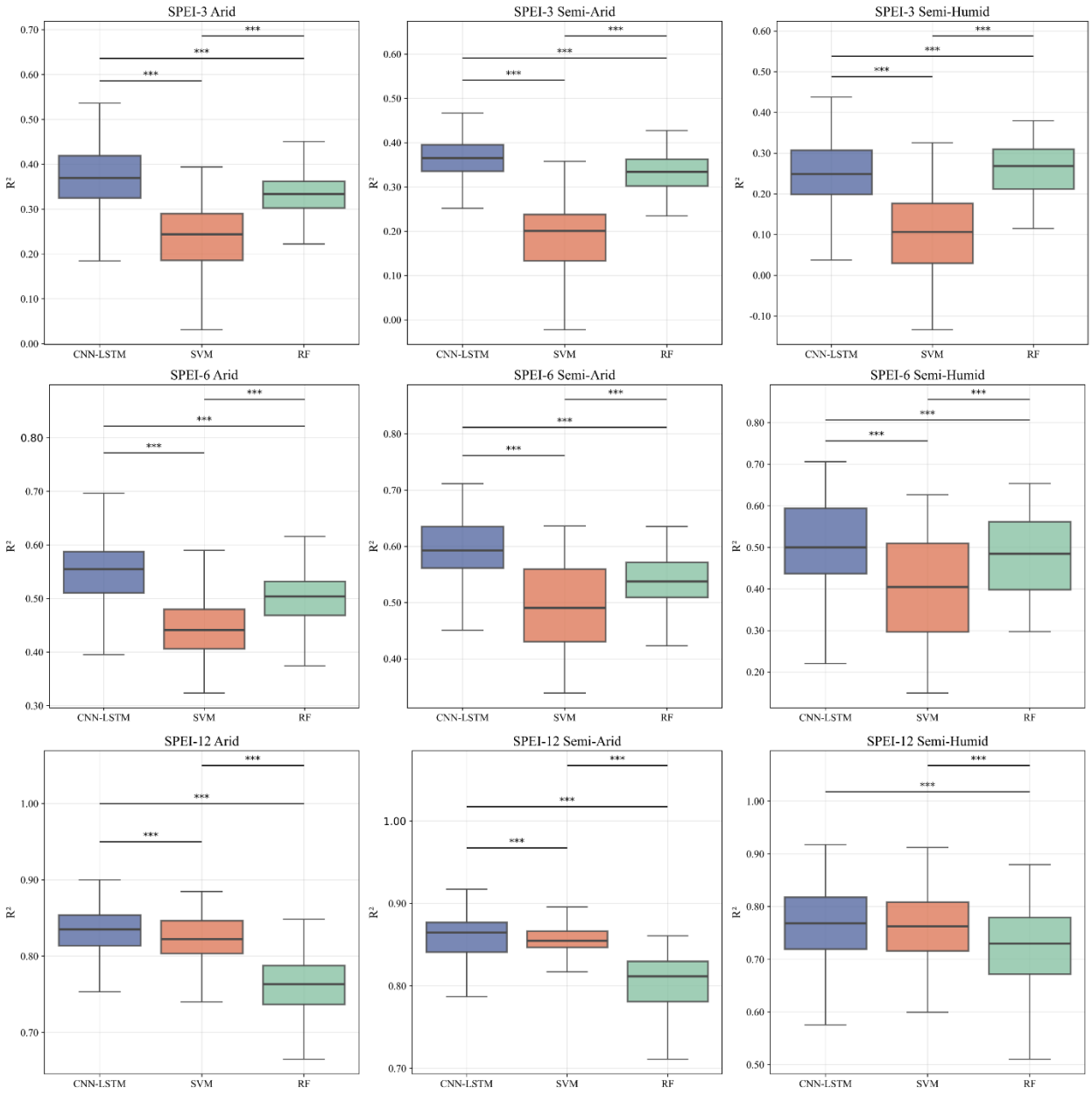

Figure 10. Comparison of predictive performance of the three models based on SPEI at different time scales. From top to bottom: 3-month (SPEI-3), 6-month (SPEI-6), and 12-month (SPEI-12) scales; from left to right: arid, semi-arid, and semi-humid regions. The boxplots show the distribution of R^2 values across models, including medians and variability ranges. Horizontal lines and asterisks (*, **, ***) indicate the significance levels of pairwise differences among models (*p<0.05, **p<0.01, ***p<0.001).

5. DISCUSSION

Based on monthly precipitation and potential evapotranspiration data from 1960 to 2022, this study calculated SPI and SPEI indices at 1-, 3-, 6-, and 12-month scales, and employed three models—Support Vector Machine (SVM), Random Forest (RF), and Convolutional Long Short-Term Memory (CNN-LSTM)—to predict meteorological drought across the semi-humid, semi-arid, and arid regions of the Loess Plateau. By comparing performance metrics including R^2, MAE, and RMSE, the study effectively revealed the applicability of different models for drought prediction. The results show that at the 1- and 3-month scales, predictive performance was generally low (particularly for SVM), indicating the difficulty of capturing short-term climate

ISSN: 2472-3703 DOI: 10.6911/WSRJ.202604_12(4).0001

variability. With increasing time scale, prediction accuracy improved significantly across all models, with CNN-LSTM consistently achieving the best performance, clearly outperforming SVM and RF. At short- to medium-term scales, RF performed better than SVM, whereas at long-term scales, SVM significantly outperformed RF. Moreover, in semi-arid and arid regions, predictions based on SPEI were generally superior to those based on SPI, likely because SPEI incorporates evapotranspiration and other meteorological factors, providing a more comprehensive representation of regional water balance. These findings are consistent with previous studies and further confirm the advantage and reliability of SPEI-based approaches for meteorological drought prediction in arid and semi-arid regions (Hou et al., 2024).

5.1. Impact of Time Scale

Fig. 11 presents the time series of SPI and SPEI from 1960 to 2022. It can be observed that as the time scale increases, the index series gradually becomes smoother. This is because at shorter time scales (e.g., 1 and 3 months), the indices mainly reflect anomalies in monthly or short-term precipitation and evapotranspiration, making them highly sensitive to extreme weather events and seasonal fluctuations, which leads to strong randomness and high-frequency variability. At longer time scales (e.g., 6 and 12 months), the indices are calculated based on cumulative precipitation and evapotranspiration, and short-term anomalies are gradually smoothed out in the accumulation process, resulting in reduced variability.The predictive performance of the three models also improved with increasing time scale. The CNN-LSTM model consistently outperformed the others at all scales, demonstrating strong adaptability and stability in drought prediction. In contrast, the performance of SVM and RF varied with time scale: at the long-term scale (12 months), SVM achieved higher prediction accuracy than RF, while at the short- to medium-term scales (3 and 6 months), RF performed significantly better than SVM. These findings further confirm that CNN-LSTM, by integrating the spatial feature extraction capability of CNN with the temporal dependency modeling strength of LSTM, offers a comprehensive advantage in multi-scale drought prediction tasks. Although traditional machine learning models show strengths at specific time scales, their overall predictive performance remains inferior to that of CNN-LSTM.

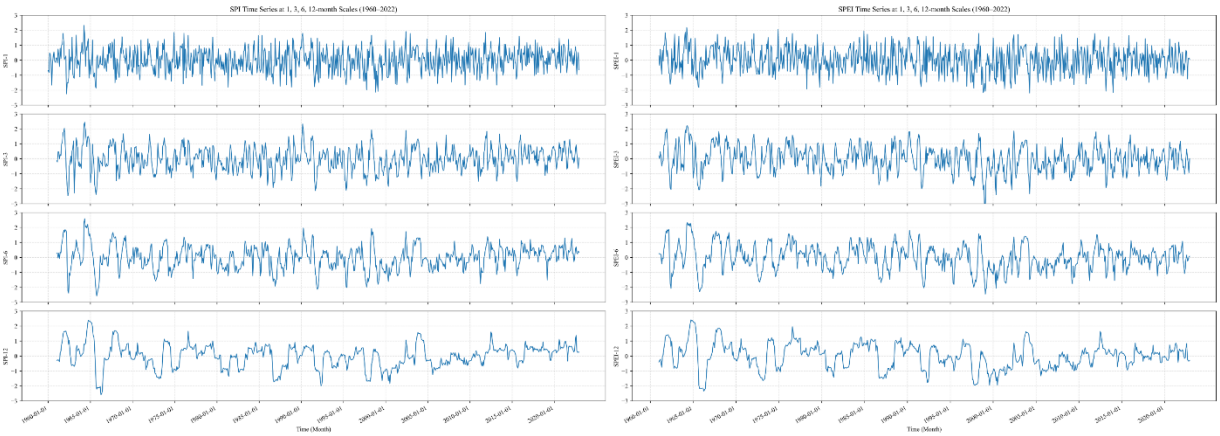

Figure 11. Time series of SPI and SPEI at different time scales: the left panel shows SPI time series at four time scales, and the right panel shows SPEI time series at four time scales.

5.2. Combined Effects of Region and Drought Index on Predictive Performance

Fig. 12 illustrates the predictive performance of the three models across different regions, indices, and time scales. The results show that in the semi-arid and semi-humid regions, SPEI consistently outperformed SPI at all time scales, as SPEI accounts for both precipitation and evapotranspiration. Since SPEI is based on the water balance (P–PET), it explicitly incorporates the contribution of potential evapotranspiration (PET) to drought formation. Compared with

ISSN: 2472-3703 DOI: 10.6911/WSRJ.202604_12(4).0001

SPI, which only reflects precipitation anomalies, SPEI better represents the actual drought process (precipitation deficit combined with increased water demand), thereby providing a more accurate characterization of drought intensity and duration and supplying stronger "effective signals" for model learning. Moreover, PET exhibits strong seasonality and interannual smoothing effects; when incorporated into the water balance, it dampens high-frequency fluctuations caused by extreme monthly precipitation, thus capturing moisture dynamics more comprehensively.

In the arid region, although SPEI outperformed SPI at short- to medium-term scales, SPI-12 achieved better performance than SPEI-12 at the long-term scale. This is mainly because SPI can more stably reflect long-term precipitation trends. Notably, when SPEI was used as the predictive indicator, the three models performed significantly better in the semi-arid and arid regions than in the semi-humid region. This result indicates that in water-limited environments, incorporating evapotranspiration enhances the predictability of drought indices, making it easier for models to capture the dynamics of water deficit processes. By contrast, when SPI was used as the predictive indicator, no such consistent pattern was observed, suggesting that precipitation-only indices exhibit less regional differentiation than SPEI. These findings further emphasize the importance of prioritizing SPEI over SPI for drought prediction in arid and semi-arid regions, while highlighting that the choice of drought index (SPEI or SPI) should be flexibly determined based on regional hydrological characteristics and prediction objectives.

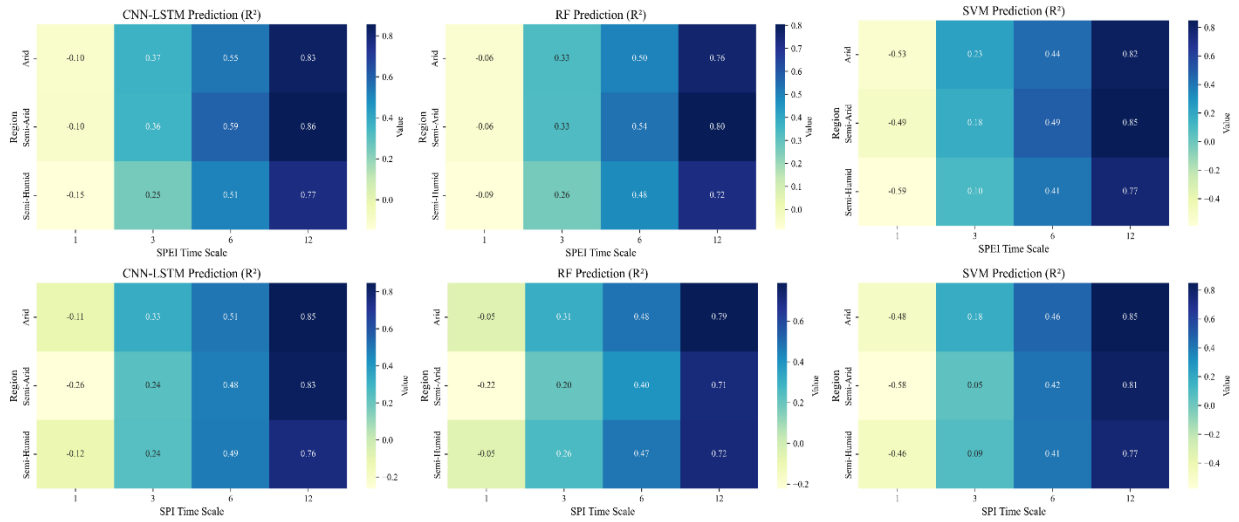

Figure 12. Predictive performance of the three models: the top row shows comparative results of CNN-LSTM, RF, and SVM based on SPEI, while the bottom row shows corresponding results based on SPI.

5.3. Influence of Model Characteristics

The differences in predictive performance of the three models across regions and time scales are closely related to their intrinsic mechanisms and overfitting behavior. The CNN-LSTM model integrates the local feature extraction capability of Convolutional Neural Networks (CNN) with the temporal dependency modeling strength of Long Short-Term Memory (LSTM) networks, enabling it to effectively capture the complex spatiotemporal dynamics of drought indices and thus achieve the best overall performance. Its loss curve converged rapidly, and no obvious divergence between training and validation sets was observed, suggesting a low risk of overfitting. This can be attributed to the use of regularization mechanisms and the relative stationarity of medium- to long-term sequences. The Random Forest (RF) model relies on an ensemble of multiple decision trees to represent nonlinear relationships and evaluates generalization performance automatically through out-of-bag (OOB) samples. The OOB error

ISSN: 2472-3703 DOI: 10.6911/WSRJ.202604_12(4).0001

curve shows that the error decreases with the number of trees and eventually stabilizes, with no signs of overfitting, indicating particularly robust performance at long-term scales. The Support Vector Machine (SVM) model maps nonlinear relationships through kernel functions. Its learning curve demonstrates that testing error decreases and stabilizes as the number of training samples increases, implying that the risk of overfitting diminishes under large-sample conditions; however, at short- to medium-term scales, the model remains limited by the volatility of the sequences.

Overall, CNN-LSTM demonstrates strong spatiotemporal modeling and generalization capabilities, RF maintains stability through the OOB mechanism, and SVM shows advantages under long-term scales and large-sample conditions. Importantly, the training diagnostics of all three models revealed no significant overfitting, confirming the robustness and reliability of the prediction results. Fig. 13 presents the CNN-LSTM loss curve, the RF OOB error curve, and the SVM learning curve, providing an intuitive illustration of model convergence, generalization capability, and overfitting risk during training

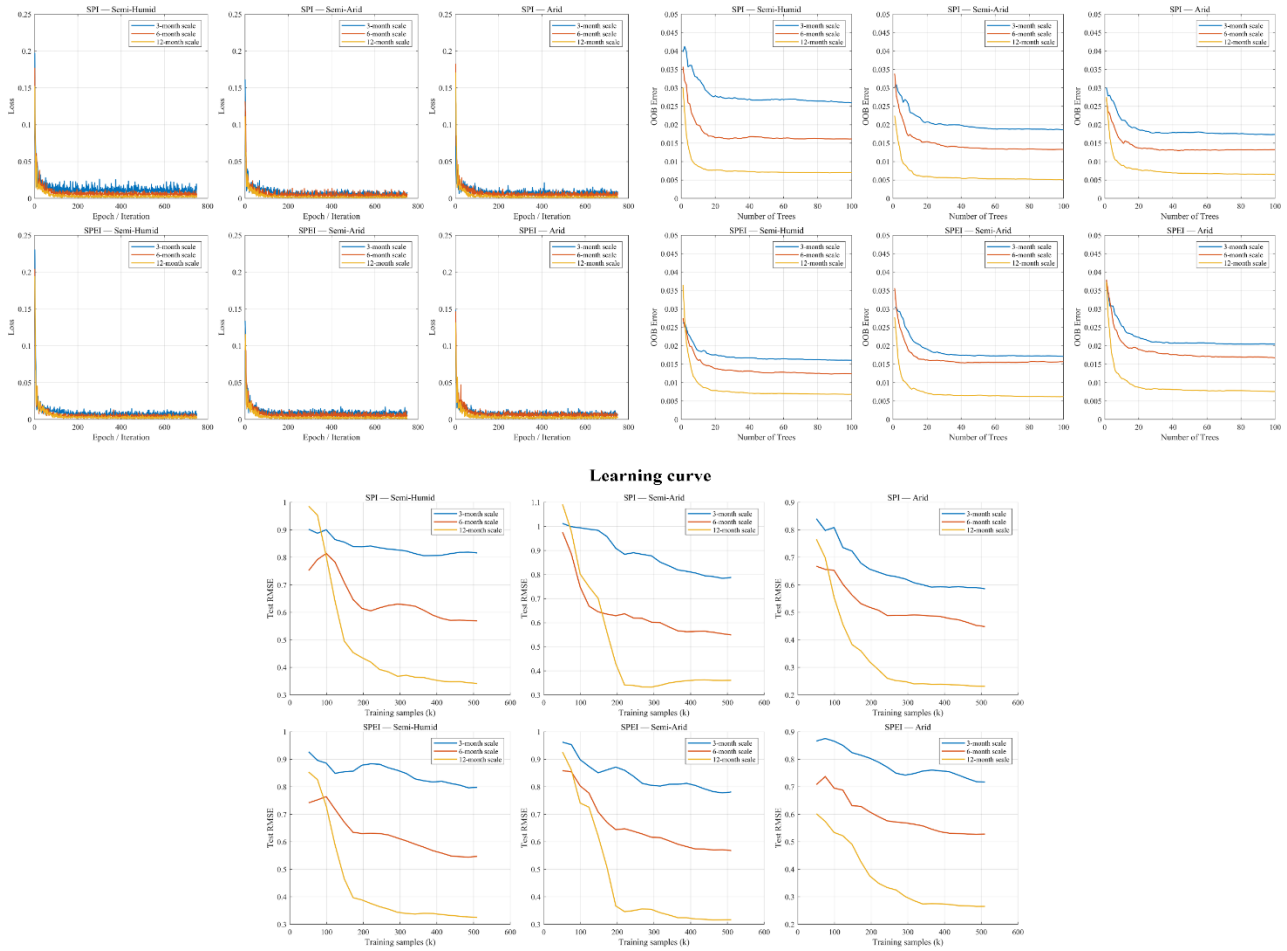

Figure 13. Diagnostic curves of CNN-LSTM, RF, and SVM models during training: the top row shows the loss function curve of the CNN-LSTM model (left) and the out-of-bag (OOB) error curve of the RF model (right), while the bottom row shows the learning curve of the SVM model.

6. CONCLUSION

Based on monthly precipitation (PRE) and potential evapotranspiration (PET) data from 1960 to 2022, this study calculated multi-scale SPI and SPEI indices and systematically evaluated the drought prediction performance of CNN-LSTM, Random Forest (RF), and Support

ISSN: 2472-3703 DOI: 10.6911/WSRJ.202604_12(4).0001

Vector Machine (SVM) models in the arid, semi-arid, and semi-humid regions of the Loess Plateau. The results show that CNN-LSTM achieved the best performance across all regions and time scales (with SPEI overall superior to SPI), consistently obtaining the highest R^2 and lowest error metrics, highlighting its advantage in modeling complex spatiotemporal dependencies. RF outperformed SVM at short- to medium-term scales (3 and 6 months), whereas SVM performed better than RF at the long-term scale (12 months). Overall, the ranking was CNN-LSTM > RF > SVM for short- to medium-term scales, and CNN-LSTM > SVM > RF for long-term scales.At the index level, the predictive accuracy of the three models under SPEI was generally higher than that under SPI, particularly in semi-arid and semi-humid regions, indicating that the introduction of evapotranspiration enhanced the ability of drought indices to represent regional water balance. However, in the arid region at the long-term scale, SPI-12 outperformed SPEI-12, suggesting that in extremely water-scarce areas, long-term precipitation trends provide a more stable explanation of drought variation than the water balance driven by evapotranspiration.At the regional level, when SPEI was used as the predictor, predictive performance in semi-arid and arid regions was significantly better than in the semi-humid region, whereas SPI did not exhibit such a pattern, further emphasizing the necessity of prioritizing SPEI in water-limited regions.

A comprehensive comparison revealed regional differences in the optimal prediction combinations. In the semi-arid and semi-humid regions, CNN-LSTM combined with SPEI outperformed CNN-LSTM combined with SPI, with CNN-LSTM + SPEI-12 achieving the best performance by fully utilizing the smoothed and stable temporal characteristics of SPEI and the strong spatiotemporal modeling capacity of CNN-LSTM. In the arid region, CNN-LSTM + SPEI was superior at short- to medium-term scales, while CNN-LSTM + SPI-12 was more advantageous at the long-term scale, indicating that in extremely water-scarce environments, precipitation-dominated SPI provides a more stable explanation of long-term drought evolution.Overall, CNN-LSTM demonstrated significant advantages across all regions and time scales, making it the optimal model for regional drought prediction. At the same time, in short- to medium-term prediction, combining RF or configurations such as SPEI-3/6 can also serve as useful supplements, providing more scientific and reliable support for drought monitoring, agricultural management, and water resource regulation in the Loess Plateau.

It is worth emphasizing that this study not only compared the predictive performance of different models and drought indices from an academic perspective but also provides direct practical value for regional drought management. The results indicate that the CNN-LSTM + SPEI combination outperformed CNN-LSTM + SPI in the semi-arid and semi-humid regions, with CNN-LSTM + SPEI-12 achieving the best overall performance, whereas CNN-LSTM + SPI-12 was more advantageous for long-term drought prediction in the arid region. These findings provide a scientific basis for constructing region-specific drought prediction systems. In practical applications, the outcomes of this study can be embedded into regional drought early warning systems, where real-time meteorological data can be used to calculate SPI/SPEI and fed into the optimal model to achieve dynamic prediction and rolling updates of drought severity. This approach can support decision-making for agricultural scheduling, water resource optimization, and drought risk management. Moreover, promoting the combined use of the CNN-LSTM model with SPEI/SPI in high-risk drought regions can serve as an important tool for meteorological and water resource management agencies, enhancing the foresight and precision of drought monitoring. Future work may further integrate remote sensing observations and in-situ soil moisture measurements to develop a deep learning–based multi-source data fusion early warning platform, thereby facilitating the translation of research findings into practical applications.

ISSN: 2472-3703 DOI: 10.6911/WSRJ.202604_12(4).0001

ACKNOWLEDGMENTS

We gratefully acknowledge the support of the National Natural Science Foundation of China (grant numbers 42261023), Key research and development program of ecological civilization construction of Gansu province (24YFFA063) and Lanzhou Youth Science and Technology Talent Innovation Project (2023-QN-123).

DISCLOSURE STATEMENT

No potential conflict of interest was reported by the author(s).

AUTHOR CONTRIBUTIONS

Yingqiang Li: Data processing, research framework development, and manuscript writing. Wei Wei: Conceptualization, methodology, and software implementation. Fei Gao: Visualization and supervision. Liang Zhou: Data processing and writing – review and editing. Dang Lu: Data curation and software. Junju Zhou: Supervision and software. Yongze Song: Validation of calculation results and original draft preparation. Mohsen Sherif: Data curation and writing – review and editing. Xiangyu Wang: Writing – reviewing and editing. Ashraf Dewan: Software and visualization.

DATA AVAILABILITY STATEMENT

The data used in this study are publicly available. The data sources used in this paper are described in Section 2.2. The precipitation (PRE) raster data are sourced from the National Tibetan Plateau Data Center (https://data.tpdc.ac.cn/zh-hans/data/faae7605-a0f2-4d18-b28f-5cee413766a2); the potential evapotranspiration (PET) raster data are also sourced from the National Tibetan Plateau Data Center (https://data.tpdc.ac.cn/zh-hans/data/8b11da09-1a40-4014-bd3d-2b86e6dccad4/).

REFERENCES

[1] Acharki, S., Singh, S. K., do Couto, E. V., Arjdal, Y., & Elbeltagi, A. (2023). Spatio-temporal distribution and prediction of agricultural and meteorological drought in a Mediterranean coastal watershed via GIS and machine learning. Physics and Chemistry of the Earth, Parts A/B/C, 131, 103425. https://doi.org/10.1016/j.pce.2023.103425.

[2] AhmadEbrahimpour, E., Aminnejad, B., & Khalili, K. (2018). Application of global precipitation dataset for drought monitoring and forecasting over the Lake Urmia basin with the GA-SVR model. International Journal of Water, 12(3), 262. https://doi.org/10.1504/ijw.2018.093674.

[3] Allen, R. G., Pereira, L. S., Raes, D., & Smith, M. (1998). Crop evapotranspiration-Guidelines for computing crop water requirements-FAO Irrigation and drainage paper 56. Fao, Rome, 300(9), D05109.

[4] Almikaeel, W., Čubanová, L., & Šoltész, A. (2022). Hydrological Drought Forecasting Using Machine Learning—Gidra River Case Study. Water, 14(3), 387. https://doi.org/10.3390/w14030387.

[5] Alsubih, M., Mallick, J., Talukdar, S., Salam, R., AlQadhi, S., Fattah, Md. A., & Thanh, N. V. (2021). An investigation of the short-term meteorological drought variability over Asir Region of Saudi Arabia. Theoretical and Applied Climatology, 145(1–2), 597–617. https://doi.org/10.1007/s00704-021-03647-4.

[6] Belayneh, A., Adamowski, J., Khalil, B., & Ozga-Zielinski, B. (2014). Long-term SPI drought forecasting in the Awash River Basin in Ethiopia using wavelet neural network and wavelet support

ISSN: 2472-3703 DOI: 10.6911/WSRJ.202604_12(4).0001

vector regression models. Journal of Hydrology, 508, 418–429. https://doi.org/10.1016/j.jhydrol.2013.10.052.

[7] Buttafuoco, G., Caloiero, T., & Coscarelli, R. (2014). Analyses of Drought Events in Calabria (Southern Italy) Using Standardized Precipitation Index. Water Resources Management, 29(2), 557–573. https://doi.org/10.1007/s11269-014-0842-5.

[8] Chiang, F., Mazdiyasni, O., & AghaKouchak, A. (2021). Evidence of anthropogenic impacts on global drought frequency, duration, and intensity. Nature Communications, 12(1). https://doi.org/10.1038/s41467-021-22314-w.

[9] Cortes, Corinna, and Vladimir Vapnik. "Support-vector networks." Machine learning 20.3 (1995): 273-297.

[10] Dixit, S., & Jayakumar, K. V. (2021). A study on copula-based bivariate and trivariate drought assessment in Godavari River basin and the teleconnection of drought with large-scale climate indices. Theoretical and Applied Climatology, 146(3–4), 1335–1353. https://doi.org/10.1007/s00704-021-03792-w.

[11] Dong, T. (2016). Study on Remote Sensing-based Drought Monitoring Method derived from Multi-Source Data. (Doctoral dissertation, Wuhan University).

[12] Feng, P., Wang, B., Liu, D. L., Waters, C., & Yu, Q. (2019). Incorporating machine learning with biophysical model can improve the evaluation of climate extremes impacts on wheat yield in south-eastern Australia. Agricultural and Forest Meteorology, 275, 100–113. https://doi.org/10.1016/j.agrformet.2019.05.018.

[13] Hargreaves, G. H., & Samani, Z. A. (1982). Estimating Potential Evapotranspiration. Journal of the Irrigation and Drainage Division, 108(3), 225–230. https://doi.org/10.1061/jrcea4.0001390.

[14] George H. Hargreaves, & Zohrab A. Samani. (1985). Reference Crop Evapotranspiration from Temperature. Applied Engineering in Agriculture, 1(2), 96–99. https://doi.org/10.13031/2013.26773.

[15] Hao, Z., Hao, F., Singh, V. P., Xia, Y., Ouyang, W., & Shen, X. (2016). A theoretical drought classification method for the multivariate drought index based on distribution properties of standardized drought indices. Advances in Water Resources, 92, 240–247. https://doi.org/10.1016/j.advwatres.2016.04.010.

[16] He, L., Wang, J., Ciais, P., Ballantyne, A., Yu, K., Zhang, W., Xiao, J., Ritter, F., Liu, Z., Wang, X., Li, X., Peng, S., Ma, C., Zhou, C., Li, Z.-L., Xie, Y., & Ye, J.-S. (2023). Non-symmetric responses of leaf onset date to natural warming and cooling in northern ecosystems. PNAS Nexus, 2(9). https://doi.org/10.1093/pnasnexus/pgad308.

[17] He, L., Wang, J., Peñuelas, J., Zohner, C. M., Crowther, T. W., Fu, Y., Zhang, W., Xiao, J., Liu, Z., Wang, X., Li, J.-H., Li, X., Peng, S., Xie, Y., Ye, J.-S., Zhou, C., & Li, Z.-L. (2024). Asymmetric temperature effect on leaf senescence and its control on ecosystem productivity. PNAS Nexus, 3(11). https://doi.org/10.1093/pnasnexus/pgae477.

[18] He, L., Wang, J., Peltier, D. M. P., Ritter, F., Ciais, P., Peñuelas, J., Xiao, J., Crowther, T. W., Li, X., Ye, J.-S., Sasaki, T., Zhou, C., & Li, Z.-L. (2025). Lagged precipitation effects on plant production across terrestrial biomes. Nature Ecology & Evolution, 9(10), 1800–1811. https://doi.org/10.1038/s41559-025-02806-4.

[19] Hou, zhaojun, Wang, B., Zhang, Y., Zhang, J., & Song, J. (2024). Drought Prediction in Jilin Province Based on Deep Learning and Spatio-Temporal Sequence Modeling. https://doi.org/10.2139/ssrn.4737903.

ISSN: 2472-3703 DOI: 10.6911/WSRJ.202604_12(4).0001

[20] Husak, G. J., Michaelsen, J., & Funk, C. (2006). Use of the gamma distribution to represent monthly rainfall in Africa for drought monitoring applications. International Journal of Climatology, 27(7), 935–944. https://doi.org/10.1002/joc.1441.

[21] Jiao, W., Wang, L., Smith, W. K., Chang, Q., Wang, H., & D'Odorico, P. (2021). Observed increasing water constraint on vegetation growth over the last three decades. Nature Communications, 12(1). https://doi.org/10.1038/s41467-021-24016-9.

[22] LeCun, Y., Bengio, Y., & Hinton, G. (2015). Deep learning. Nature,521(7553), 436-444..

[23] Li, J., Wang, Z., Wu, X., Xu, C., Guo, S., Chen, X., & Zhang, Z. (2021). Robust Meteorological Drought Prediction Using Antecedent SST Fluctuations and Machine Learning. Water Resources Research, 57(8). Portico. https://doi.org/10.1029/2020wr029413.

[24] Li, M., Zhou, Q., Han, X., & Lv, P. (2024). Prediction of reference crop evapotranspiration based on improved convolutional neural network (CNN) and long short-term memory network (LSTM) models in Northeast China. Journal of Hydrology, 645, 132223. https://doi.org/10.1016/j.jhydrol.2024.132223.

[25] Li, Z., Zheng, F.-L., & Liu, W.-Z. (2012). Spatiotemporal characteristics of reference evapotranspiration during 1961–2009 and its projected changes during 2011–2099 on the Loess Plateau of China. Agricultural and Forest Meteorology, 154–155, 147–155. https://doi.org/10.1016/j.agrformet.2011.10.019.

[26] Liu, W., & Sang, T. (2013). Potential productivity of the Miscanthus energy crop in the Loess Plateau of China under climate change. Environmental Research Letters, 8(4), 044003. https://doi.org/10.1088/1748-9326/8/4/044003.

[27] Liu, Z., Wang, Y., Shao, M., Jia, X., & Li, X. (2016). Spatiotemporal analysis of multiscalar drought characteristics across the Loess Plateau of China. Journal of Hydrology, 534, 281–299. https://doi.org/10.1016/j.jhydrol.2016.01.003.

[28] Manzano, A., Clemente, M. A., Morata, A., Luna, M. Y., Beguería, S., Vicente-Serrano, S. M., & Martín, M. L. (2019). Analysis of the atmospheric circulation pattern effects over SPEI drought index in Spain. Atmospheric Research, 230, 104630. https://doi.org/10.1016/j.atmosres.2019.104630.

[29] McKee, T. B., Doesken, N. J., & Kleist, J. (1993). The relationship of drought frequency and duration to time scales. In Proceedings of the 8th Conference on Applied Climatology (Vol. 17, No. 22, pp. 179-183).

[30] Mishra, A. K., & Singh, V. P. (2010). A review of drought concepts. Journal of Hydrology, 391(1–2), 202–216. https://doi.org/10.1016/j.jhydrol.2010.07.012.

[31] Potop, V., Boroneanţ, C., Možný, M., Štěpánek, P., & Skalák, P. (2013). Observed spatiotemporal characteristics of drought on various time scales over the Czech Republic. Theoretical and Applied Climatology, 115(3–4), 563–581. https://doi.org/10.1007/s00704-013-0908-y.

[32] Schreiner-McGraw, A. P., & Ajami, H. (2021). Delayed response of groundwater to multi-year meteorological droughts in the absence of anthropogenic management. Journal of Hydrology, 603, 126917. https://doi.org/10.1016/j.jhydrol.2021.126917.

[33] Şener, İ. F., & Tuğal, İ. (2025). Optimized CNN-LSTM with hybrid metaheuristic approaches for solar radiation forecasting. Case Studies in Thermal Engineering, 72, 106356. https://doi.org/10.1016/j.csite.2025.106356.

[34] Shahnazi, S., Roushangar, K., & Hashemi, H. (2025). A novel implementation of pre-processing approaches and hybrid kernel-based model for short- and long-term groundwater drought forecasting. Journal of Hydrology, 652, 132667. https://doi.org/10.1016/j.jhydrol.2025.132667.

ISSN: 2472-3703 DOI: 10.6911/WSRJ.202604_12(4).0001

[35] Sun, L. (2009). Blended drought indices for agricultural drought: risk assessment on the Canadian prairies. https://doi.org/10.22215/etd/2009-08724.

[36] Vicente-Serrano, S. M., Beguería, S., & López-Moreno, J. I. (2010). A Multiscalar Drought Index Sensitive to Global Warming: The Standardized Precipitation Evapotranspiration Index. Journal of Climate, 23(7), 1696–1718. https://doi.org/10.1175/2009jcli2909.1.

[37] Wu, Z., Yin, H., He, H., & Li, Y. (2022). Dynamic-LSTM hybrid models to improve seasonal drought predictions over China. Journal of Hydrology, 615, 128706. https://doi.org/10.1016/j.jhydrol.2022.128706.

[38] Xu, D., Zhang, Q., Ding, Y., & Zhang, D. (2021a). Application of a hybrid ARIMA-LSTM model based on the SPEI for drought forecasting. Environmental Science and Pollution Research, 29(3), 4128–4144. https://doi.org/10.1007/s11356-021-15325-z.

[39] Xu, D., Zhang, Q., Ding, Y., & Huang, H. (2020). Application of a Hybrid ARIMA–SVR Model Based on the SPI for the Forecast of Drought—A Case Study in Henan Province, China. Journal of Applied Meteorology and Climatology, 59(7), 1239–1259. https://doi.org/10.1175/jamc-d-19-0270.1.

[40] Xu, D., Zhang, Q., Ding, Y., & Zhang, D. (2021b). Spatiotemporal Pattern Mining of Drought in the Last 40 Years in China Based on the SPEI and Space–Time Cube. Journal of Applied Meteorology and Climatology, 60(9), 1219–1230. https://doi.org/10.1175/jamc-d-21-0049.1.

[41] Xu, H., Wang, X., Zhao, C., Shan, S., & Guo, J. (2021c). Seasonal and aridity influences on the relationships between drought indices and hydrological variables over China. Weather and Climate Extremes, 34, 100393. https://doi.org/10.1016/j.wace.2021.100393.

[42] Xu, Q., Jia, Q., Li, Y., Zhang, H., & Ren, P. (2025). A self-attention convolutional long and short-term memory network for correcting sea surface wind field forecasts to facilitate sea ice drift prediction. Computers & Geosciences, 205, 105997. https://doi.org/10.1016/j.cageo.2025.105997.

[43] Xu, Y., Zhang, X., Hao, Z., Hao, F., & Li, C. (2021a). Projections of future meteorological droughts in China under CMIP6 from a three-dimensional perspective. Agricultural Water Management, 252, 106849. https://doi.org/10.1016/j.agwat.2021.106849.

[44] Yuan, X., Zhang, M., Wang, L., & Zhou, T. (2017). Understanding and seasonal forecasting of hydrological drought in the Anthropocene. Hydrology and Earth System Sciences, 21(11), 5477–5492. https://doi.org/10.5194/hess-21-5477-2017.

[45] Zhang, B., Wu, P., Zhao, X., Wang, Y., Wang, J., & Shi, Y. (2012). Drought variation trends in different subregions of the Chinese Loess Plateau over the past four decades. Agricultural Water Management, 115, 167–177. https://doi.org/10.1016/j.agwat.2012.09.004.

[46] Zhang, Q., Miao, C., Gou, J., & Zheng, H. (2023). Spatiotemporal characteristics and forecasting of short-term meteorological drought in China. Journal of Hydrology, 624, 129924. https://doi.org/10.1016/j.jhydrol.2023.129924.

[47] Zhang, X., Duan, Y., Duan, J., Chen, L., Jian, D., Lv, M., Yang, Q., & Ma, Z. (2022). A daily drought index-based regional drought forecasting using the Global Forecast System model outputs over China. Atmospheric Research, 273, 106166. https://doi.org/10.1016/j.atmosres.2022.106166.

[48] Zhang, Y., Ma, Y., Fang, H., & Wang, H. (2025). Investigation on forecast of offshore wind power generation hybrid attention mechanism and bi-directional long short-term memory based on deep learning. Ocean & Coastal Management, 270, 107884. https://doi.org/10.1016/j.ocecoaman.2025.107884.

ISSN: 2472-3703 DOI: 10.6911/WSRJ.202604_12(4).0001

[49] Zhao, G., Tu, X. J., Wang, T. (2021). Drought prediction based on artificial neural network and support vector machine. Pearl River, 42(4), 1–9. https://doi.org/10.3969/j.issn.1001-9235.2021.04.001.